

Exploring the topology induced by non-Markovian Liouvillian exceptional points

Hao-Long Zhang^{1,*}, Yan Wang^{1,*}, Wen Ning^{1,*}, Shou-Bang Yang¹, Jia-Hao Lü¹, Fan Wu¹, Pei-Rong Han^{2,†}, Li-Hua Lin^{1,3}, Zhen-Biao Yang^{1,3,‡} and Shi-Biao Zheng^{1,3§}

¹*Fujian Key Laboratory of Quantum Information and Quantum Optics, College of Physics and Information Engineering, Fuzhou University, Fuzhou 350108, China*

²*School of Physics and Mechanical and Electrical Engineering, Longyan University, Longyan 364012, China*

³*Hefei National Laboratory, Hefei 230088, China*

(Dated: December 9, 2025)

Non-Hermitian (NH) systems can display exotic topological phenomena without Hermitian counterparts, enabled by exceptional points (EPs). So far, investigations of NH topology have been restricted to EPs of the NH Hamiltonian, which governs the system dynamics conditional upon no quantum jumps occurring. The Liouvillian superoperator, which combines the effects of quantum jumps with NH Hamiltonian dynamics, possesses EPs (LEPs) that are significantly different from those of the corresponding NH Hamiltonian. We here study the topological features of the LEPs in the system consisting of a qubit coupled to a non-Markovian reservoir. We find that two distinct winding numbers can be simultaneously produced by executing a single closed path encircling the twofold LEP2, formed by two coinciding LEP2s, each involving a pair of coalescing eigenvectors of the extended Liouvillian superoperator. We experimentally demonstrate this purely non-Markovian phenomenon with a circuit, where a superconducting qubit is coupled to a decaying resonator which acts as a reservoir with memory effects. The results push the exploration of exceptional topology from the Markovian to non-Markovian regime.

The behaviors of any quantum system are unavoidably affected by its surrounding environment, which can be modeled as a reservoir that contains a continuum of electromagnetic modes [1, 2]. The effects of such a reservoir can be described by a dissipator that influences the system dynamics in two ways. On the one hand, it adds a non-Hermitian (NH) term to the system Hamiltonian. On the other hand, it induces random quantum jumps, as a consequence of leakage of photons into the reservoir. When no quantum jumps occur, the system dynamics is described by an NH Hamiltonian. The most remarkable feature of the NH Hamiltonian is the presence of exceptional points (HEPs) [3–7], where both the eigenenergies and eigenvectors coalesce. The HEPs can display exotic behaviors that are inaccessible with Hermitian systems, exemplified by the exceptional topology [6–27], which can manifest either in the eigenvectors or in the complex eigenspectrum.

Recently, it was discovered that more intriguing phenomena can emerge in the eigenspectrum of the Liouvillian superoperator, where the quantum jump is incorporated with the NH Hamiltonian dynamics. The corresponding degeneracies, at which both the eigenvalues and eigenvectors of the Liouvillian superoperator coalesce, are referred to as the Liouvillian EPs (LEPs) [28–31]. The Liouvillian eigenspectrum can display much richer exceptional structures than the NH Hamiltonian eigenspectrum. For example, the Liouvillian eigenspectrum for a driven qubit in a Markovian reservoir involves exceptional lines and higher-order EPs [31], which have no counterparts in the eigenspectrum of the corresponding NH Hamiltonian. Experimentally, Markovian LEPs have

been observed in superconducting circuits [32–34] and ion traps [35], and their applications in chiral state transfer [36] and control of quantum heat engines [37, 38] have been demonstrated.

The Markovian approximation breaks down when the reservoir is structured [39, 40], e.g., an electromagnetic cavity to which an atom is coupled. Such a reservoir has a memory effect, which enables backflow of the energy and information. To account for this effect, some additional degrees of freedom of the reservoir need to be introduced, which increases the dimension of the Liouvillian superoperator and its eigenvectors. The corresponding Liouvillian eigenspectrum is fundamentally different from that associated with the Markovian reservoir, featuring coexistence of LEPs with different orders as a consequence of the memory effect [41], which has been confirmed in a very recent experiment [42].

These advancements naturally lead to the important question: What are the topological features of LEPs? So far, this question has not been explored in theory and experiment. We here investigate the topology associated with the eigenspectrum of a qubit coupled to a reservoir with the Lorentzian spectral density. We discovered that the singularity in parameter space, where all LEPs are located, is characterized by a hybrid topological invariant, which consists of different winding numbers associated with different Liouvillian eigenenergies when the control parameters are varied along a closed path enclosing these LEPs. We experimentally implement this unique topological feature with a circuit quantum electrodynamics system, where a Josephson-junction-based superconducting qubit is controllably coupled to its readout resonator

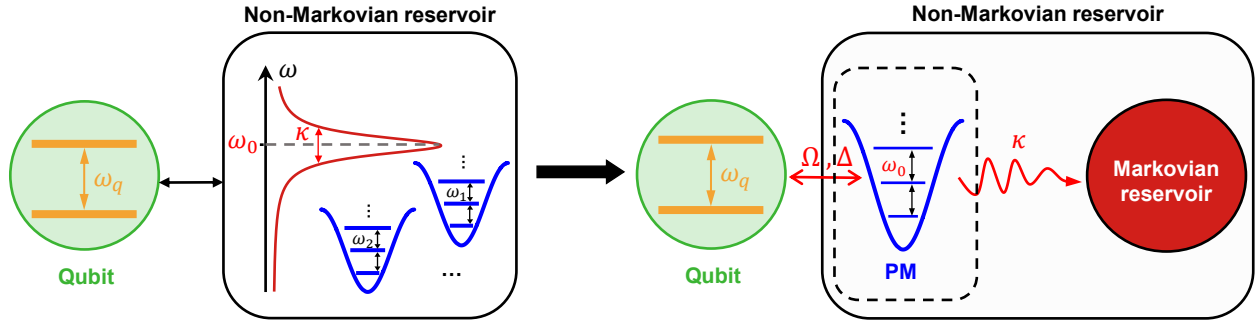


FIG. 1. (color online). Sketch of the theoretical model. A qubit with the frequency ω_q interacts with a non-Markovian reservoir containing a continuum of electromagnetic field modes with the spectral width κ and central frequency ω_0 . Such a reservoir is equivalent to a leaky cavity storing an effective photonic mode, referred to as a pseudomode (PM), with the frequency ω_0 and decaying rate κ . The coupling strength Ω and detuning $\Delta = \omega_q - \omega_0$ between the qubit and the PM serve as the control parameters of the extended Liouvillian superoperator, which governs the dynamics of the qubit-PM system.

that serves as a non-Markovian reservoir for the qubit. The coupling strength and detuning span a parameter space, where a desired cyclic path is executed by controlling the amplitude and frequency of the ac flux that mediates a sideband interaction between the qubit and the resonator.

The theoretical model consists of a qubit coupled to a reservoir composed of a continuum of electromagnetic field modes with a Lorentzian spectral density [1]

$$J(\omega) = \frac{1}{\pi} \frac{\kappa/2}{(\omega - \omega_0)^2 + (\kappa/2)^2}, \quad (1)$$

where κ represents the spectral width and ω_0 is the spectral central frequency. The memory effect of this reservoir can be captured by introducing a pseudomode (PM) with the frequency ω_0 and the decaying rate κ . In other words, the non-Markovian reservoir corresponds to a leaky cavity holding a photonic mode with the frequency ω_0 , as shown in Fig. 1. In the framework rotating at the frequency ω_0 , the evolution of the composite qubit-PM system is described by the master equation

$$\frac{d\rho}{dt} = \mathcal{L}\rho, \quad (2)$$

where \mathcal{L} is the extended Liouvillian operator, defined as

$$\mathcal{L}\rho = i \left[\rho H_{NH}^\dagger - H_{NH}\rho \right] + \kappa b\rho b^\dagger. \quad (3)$$

Here H_{NH} is the NH Hamiltonian, given by ($\hbar = 1$ is set)

$$H_{NH} = \Omega (b^\dagger |g\rangle \langle e| + b |e\rangle \langle g|) + \Delta |e\rangle \langle e| - \frac{i\kappa}{2} b^\dagger b, \quad (4)$$

where Ω and Δ are the coupling strength and detuning between the qubit and the PM, $|g\rangle$ and $|e\rangle$ represent the lower and upper levels of the qubit, and b^\dagger and b denote the creation and annihilation operators for the PM, respectively.

The system excitation, defined as $N_e = |e\rangle \langle e| + b^\dagger b$, is conserved under the NH Hamiltonian. The last term of $\mathcal{L}\rho$ describes the quantum jump, which induces a jump for the PM from the n -photon Fock state $|n\rangle$ to $|n-1\rangle$. When the qubit is initially in a superposition of $|g\rangle$ and $|e\rangle$ and the PM initially in the vacuum state $|0\rangle$, the qubit-PM evolution is restricted in the subspace with zero and one excitation: $\{|g, 0\rangle, |e, 0\rangle, |e, 1\rangle\}$, where the extended Liouvillian superoperator corresponds to a 9×9 NH matrix [41, 42], \mathcal{L}_{matrix} , whose eigenvalues and eigenvectors satisfy the secular equation

$$\mathcal{L}_{matrix} \mathbf{V}_j = \lambda_j \mathbf{V}_j, \quad (5)$$

where \mathbf{V}_j is the eigenvector with the eigenvalue λ_j . \mathcal{L}_{matrix} possesses 9 eigenvalues given by

$$\begin{aligned} \lambda_0 &= 0, \\ \lambda_{1(2)} &= \eta_{\mp} - \sqrt{\eta_{\pm}^2 - \Omega^2}, \\ \lambda_{3(4)} &= \eta_{\mp} + \sqrt{\eta_{\pm}^2 - \Omega^2}, \\ \lambda_{5(6)} &= -\frac{\kappa}{2} \pm \sqrt{\alpha + \beta}, \\ \lambda_{7(8)} &= -\frac{\kappa}{2} \pm \sqrt{\alpha - \beta}, \end{aligned} \quad (6)$$

where $\eta_{\pm} = (-\kappa \pm 2i\Delta)/4$, $\alpha = \kappa^2/8 - \Delta^2/2 - 2\Omega^2$, and $\beta = \sqrt{\alpha^2 + \Delta^2\kappa^2/4}$.

The last eight eigenvalues versus the coupling strength Ω and detuning Δ are displayed in the Supplemental Material. For $\Delta = 0$, there exist three pairs of degenerate eigenvectors \mathbf{V}_1 - \mathbf{V}_2 , \mathbf{V}_3 - \mathbf{V}_4 , and \mathbf{V}_7 - \mathbf{V}_8 (\mathbf{V}_5 - \mathbf{V}_6), irrespective of the value of Ω . When $\Omega < \kappa/4$, \mathbf{V}_7 and \mathbf{V}_8 degenerate, otherwise \mathbf{V}_5 and \mathbf{V}_6 degenerate. At the parameter-space position $\{\Omega = \kappa/4; \Delta = 0\}$, \mathbf{V}_1 (\mathbf{V}_2) and \mathbf{V}_3 (\mathbf{V}_4) coalesce, and λ_1 (λ_2) coincides with λ_3 (λ_4). In addition to featuring a twofold order-2 LEP (LEP2), this position also corresponds to an order-3 LEP (LEP3), characterized by the coalescence of three

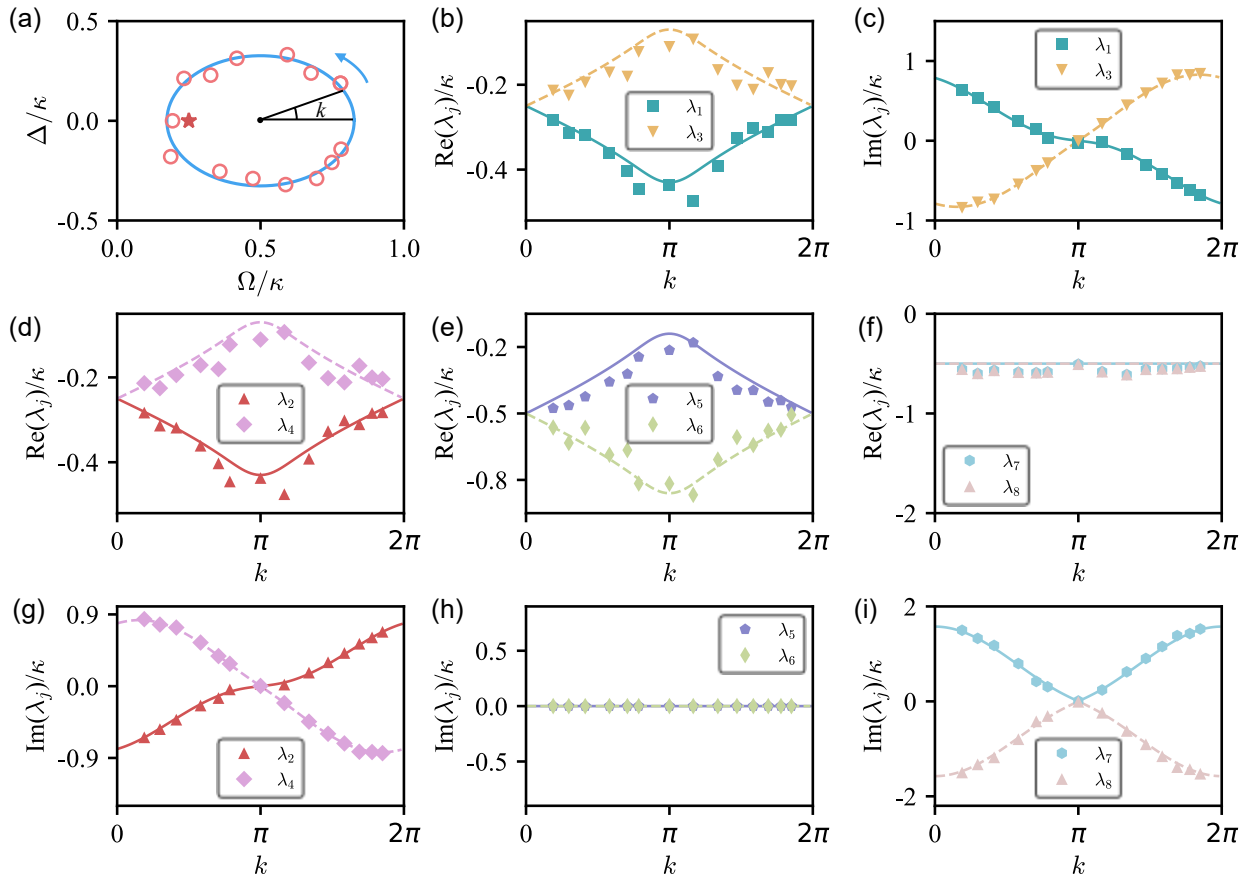


FIG. 2. (color online). Experimental measurement of the Liouvillian spectrum. (a) Parameter-space loop. We here set $\Omega = \kappa/2 + r \cos k$ and $\Delta = r \sin k$, so that the LEPs (star), located at $\{r = \kappa/4, k = \pi\}$, are enclosed in the loop when $r > \kappa/4$. (b)-(i) Measured Liouvillian eigenvalues, λ_1 to λ_8 , versus k . λ_j for each value of k is extracted by tracking the dynamical evolution of the qubit-PM system starting with the initial state $(|g\rangle + i|e\rangle)/\sqrt{2}$, and exponentially fitting the amplitude associated with the eigenvector \mathbf{V}_j , $A_j(t) = A_j(0)e^{\lambda_j t}$. All the data are measured for $r \approx 0.327\kappa$.

degenerate eigenvectors \mathbf{V}_5 , \mathbf{V}_6 , and \mathbf{V}_7 . These LEPs have been observed by a previous circuit quantum electrodynamics experiment [42], but where Δ was fixed to 0 and the topological features of these LEPs were not investigated. As shown in Eq. (6), when $\Delta \neq 0$, the degeneracies of \mathbf{V}_1 - \mathbf{V}_2 , \mathbf{V}_3 - \mathbf{V}_4 , and \mathbf{V}_7 - \mathbf{V}_8 pairs are lifted. The variation of both the parameters Ω and Δ along a cyclic path is necessary to probe the topology of the EPs.

The superconducting circuit used to probe the exceptional topology consists of a bus resonator (R_b) connecting five frequency-tunable qubits (Q_j with $j = 1$ to 5), each of which is connected to a readout resonator (R_j). In the experiment, Q_1 is used as the test qubit for constructing the LEPs, and R_1 serves as the non-Markovian reservoir, which has a Lorentzian spectral distribution with a central frequency $\omega_0/2\pi \approx 6.66$ MHz and a spectral width $\kappa \approx 5 \mu\text{s}^{-1}$. The maximum frequency of Q_1 is $\omega_{\text{max}}/2\pi \approx 6.05$ MHz. The difference between ω_0 and ω_{max} is much larger than the on-resonance coupling strength between Q_1 and the decaying photonic mode of

R_1 (PM), which has a value of $g_r \approx 2\pi \times 40$ MHz. The controllable Q_1 -PM coupling is realized with an ac flux, which modulates the frequency of the qubit as [42–44], $\omega_q = \bar{\omega} + \varepsilon \cos(\nu t)$, where $\bar{\omega}$ is the mean frequency of the qubit, and ε and ν denote the modulating amplitude and frequency, respectively. When ν is close to $\omega_0 - \bar{\omega}$, Q_1 interacts with R_1 at the first sideband with respect to the parametric modulation. The effective photon swapping rate between Q_1 and R_1 is $\Omega = g_r J_1(\mu)$, and the detuning is $\Delta = \bar{\omega} + \nu - \omega_0$, where $J_1(\mu)$ is the first-order Bessel function of the first kind with $\mu = \varepsilon/\nu$. The interplay between this coherent coupling and the incoherent photonic decay of R_1 is described by the extended Liouvillian operator \mathcal{L} of Eq. (3). The second qubit Q_2 is used as an ancilla for the readout of the output Q_1 -PM state. The other three qubits are not used and are tuned to effectively decouple from Q_1 and Q_2 throughout the experiment due to the large detunings.

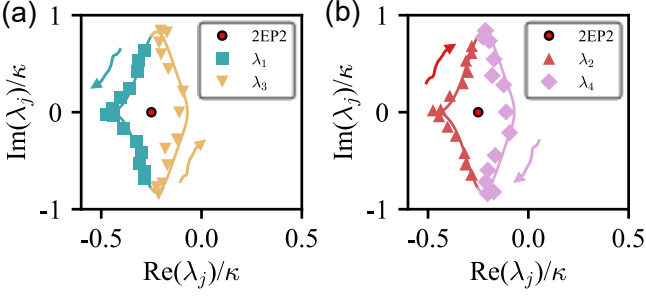


FIG. 3. (color online). Characterization of the hybrid topological invariant. Trajectories of the measured Liouvillian eigenvalues: λ_1 and λ_3 (a); λ_2 and λ_4 (b); are plotted on the complex $\text{Re}(\lambda)$ - $\text{Im}(\lambda)$ plane (in unit of κ). The control parameters are varied along the circle shown in Fig. 2. The solid lines denote the trajectories of the calculated eigenvalues.

In our experiment, the Liouvillian spectrum is extracted from the dynamically evolved output state, which can be expressed in terms of the eigenvectors of the Liouvillian superoperator

$$\mathbf{V}(t) = \sum_j A_j(t) \mathbf{V}_j, \quad (7)$$

where $A_j(t) = A_j(0)e^{\lambda_j t}$. The eigenvalue λ_j is inferred by exponentially fitting the evolution of the amplitude $A_j(t)$. When $A_j(0) = 0$, \mathbf{V}_j does not appear in the expansion of $\mathbf{V}(t)$ so that λ_j cannot be obtained from the dynamical evolution of the associated amplitude $A_j(t)$, which remains zero. Therefore, the number of eigenvalues that can be extracted depends upon the initial state. In our experiment, we choose $(|g\rangle + i|e\rangle)/\sqrt{2}$ as the initial state for Q_1 , which can be prepared from the ground state with a $\pi/2$ pulse. The resonator R_1 is initially in the vacuum state $|0\rangle$. This choice ensures that each of the eigenvectors has a nonvanishing amplitude during the state evolution for $\Delta \neq 0$. After preparation of this initial state, the parametric modulation is applied to mediate the sideband interaction between Q_1 and the PM. The effective interaction strength Ω and detuning Δ are controlled by the modulating parameters ε and ν , respectively.

Following the switch-off of the parametric modulation, it is necessary to perform the state mappings: $Q_1 \rightarrow R_b$, $R_b \rightarrow Q_2$, and $\text{PM} \rightarrow Q_1$. These operations transfer the output PM- Q_1 state to the Q_1 - Q_2 system, whose joint density matrix can be reconstructed by quantum state tomography. From the measured output density matrix, we can extract the amplitude $A_j(t)$ associated with the eigenvector \mathbf{V}_j of the extended Liouvillian superoperator. The corresponding eigenvalue λ_j is inferred by exponentially fitting the data of A_j measured for different Q_1 -PM interaction times.

To reveal the topology of the complex eigenspectrum, it is necessary to map out the corresponding eigenenergies

along a circuit in the parameter space $\{\Omega, \Delta\}$. We choose circular loops centered at $\{\Omega = \kappa/2; \Delta = 0\}$. With this setting, we can rewrite the two control parameters as $\Omega = \kappa/2 + r \cos k$ and $\Delta/2 = r \sin k$, and the LEPs are enclosed in the loop when $r > \kappa/4$. In our experiment, the topology is demonstrated with the choice $r = 0.327\kappa$, as shown in Fig. 2(a). Fig. 2(b)-(i) display the eigenvalues λ_j for $j = 1$ to 8, inferred by exponential fitting of $A_j(t)$ for different values of k (see Supplemental Material for details). The eigenvalue λ_j is inferred by the fitted amplitude associated with the eigenvector \mathbf{V}_j .

The spectral topology is manifested on the complex $\text{Re} \lambda$ - $\text{Im} \lambda$ plane. The winding number associated with λ_j is defined as [8, 18]

$$\mathcal{W}_j = \frac{1}{2m\pi} \int_0^{2m\pi} dk \partial_k \arg[\lambda_j(k) - \lambda_{\text{EP}}], \quad (8)$$

where m is the smallest positive integer that satisfies the condition $\lambda_j(k + 2m\pi) = \lambda_j(k)$. The absolute value of \mathcal{W}_j counts the number of times that the eigenvalue λ_j winds around the EP on the complex plane, and its sign denotes the moving direction of λ_j when k is varied from 0 to $2m\pi$. Fig. 3(a) presents the measured eigenvalues λ_1 and λ_3 on the complex plane, which well agree with the ideal results (solid lines). As expected, when k is varied from 0 to 2π , the combination of the paths traversed by λ_1 and λ_3 forms a loop enclosing the degenerate eigenvalue $\lambda_{\text{LEP2}} = -\kappa/4$ at the twofold LEP2. At $k = 2\pi$, an exchange of eigenvalues is completed, that is, λ_1 (λ_3) is moved to the original position of λ_3 (λ_1). As the variation of the control parameters for $k = 2\pi$ to 4π is identical to that for $k = 0$ to 2π , the trajectory traversed by λ_3 (λ_1) during $k = 0$ to 2π corresponds to that by λ_1 (λ_3) during the interval from $k = 2\pi$ to 4π . In other words, during $k = 0$ to 4π these two eigenvalues are exchanged for two times, traversing a closed path that encloses the LEP2. This implies that the corresponding winding numbers are $\mathcal{W}_1 = \mathcal{W}_3 = 1/2$. Fig. 3(b) displays the measured eigenvalues λ_2 and λ_4 on the $\text{Re} \lambda$ - $\text{Im} \lambda$ plane. The trajectories traversed by λ_2 and λ_4 also form a loop that has the same shape but opposite direction as compared with that formed by the paths of λ_1 and λ_3 . Consequently, $\mathcal{W}_2 = \mathcal{W}_4 = -1/2$. Such a hybrid winding number is a unique feature of the twofold LEP2, which is formed by two overlapping LEP2s, one characterizing the coalescence of the eigenvectors \mathbf{V}_1 and \mathbf{V}_3 , while the other featuring the coincidence between \mathbf{V}_2 and \mathbf{V}_4 .

The most remarkable topological feature of the system is that the winding numbers associated with trajectories traversed by $\lambda_{1(3)}$ and $\lambda_{2(4)}$ have the opposite values. This implies that the twofold LEP2 has a hybrid topological invariant, which can be either $1/2$ or $-1/2$, depending on which pair of eigenvalues is used to extract the winding number. This exotic feature distinguishes the topological phenomena of the non-Markovian LEP2

from those of the corresponding HEP2, which has a definite winding number. This hybrid topological invariant is fundamentally different from that possessed by the exceptional nexus [12], which manifests as distinct winding numbers associated with Berry phases accumulated by cyclic paths on different complex planes of the control parameters. In the present system, opposite winding numbers are produced by the same cyclic path in parameter space. Such an intriguing exceptional topological phenomenon is a purely non-Markovian effect, which emerges only when the information transferred to the PM of the reservoir can flow back to the qubit and be extracted. Unlike the LEP2, the LEP3 does not exhibit any topological feature, as shown in the Supplemental Material.

In conclusion, we have explored the topological phenomena of Liouvillian EPs of a qubit coupled to a non-Markovian reservoir in a superconducting circuit. The topology is encoded in the Liouvillian spectrum in parameter space, which is mapped out by fitting the evolutions of the amplitudes associated with the eigenvectors of the extended Liouvillian superoperator. The twofold LEP2, which is a consequence of the non-Markovianity, possesses a hybrid topological invariant, manifested by opposite winding numbers associated with the two LEP2s that coincide with each other both in the parameter space and on the complex spectrum plane, but carry opposite topological charges. Our work paves the way for the exploration of exotic topological phenomena associated with non-Markovian quantum EPs.

Acknowledgments—This work was supported by the National Natural Science Foundation of China (Grants No. 12474356, No. 12475015, No. 12274080, No. 12505021, No. 12505016), Quantum Science and Technology-National Science and Technology Major Project (Grant No. 2021ZD0300200), and the Natural Science Foundation of Fujian Province (Grants No. 2025J01383, No. 2025J01465).

Data availability—The data that support the findings of this article are not publicly available. The data are available from the authors upon reasonable request.

Mater. **18**, 783 (2019).

- [4] M.-A. Miri and A. Al, Exceptional points in optics and photonics, *Science* **363**, eaar7709 (2019).
- [5] Z. G. Yuto Ashida and M. Ueda, Non-Hermitian physics, *Adv. Phys.* **69**, 249 (2020).
- [6] H. Shen, B. Zhen, and L. Fu, Topological band theory for non-Hermitian Hamiltonians, *Phys. Rev. Lett.* **120**, 146402 (2018).
- [7] Z. Gong, Y. Ashida, K. Kawabata, K. Takasan, S. Higashikawa, and M. Ueda, Topological phases of non-Hermitian systems, *Phys. Rev. X* **8**, 031079 (2018).
- [8] Q.-B. Zeng, Y.-B. Yang, and Y. Xu, Topological phases in non-Hermitian aubry-andré-harper models, *Phys. Rev. B* **101**, 020201 (2020).
- [9] E. J. Bergholtz, J. C. Budich, and F. K. Kunst, Exceptional topology of non-Hermitian systems, *Rev. Mod. Phys.* **93**, 015005 (2021).
- [10] K. Ding, C. Fang, and G. Ma, Non-Hermitian topology and exceptional-point geometries, *Nat. Rev. Phys.* **4**, 745 (2022).
- [11] C. Dembowski, H.-D. Gräf, H. L. Harney, A. Heine, W. D. Heiss, H. Rehfeld, and A. Richter, Experimental observation of the topological structure of exceptional points, *Phys. Rev. Lett.* **86**, 787 (2001).
- [12] W. Tang, X. Jiang, K. Ding, Y.-X. Xiao, Z.-Q. Zhang, C. T. Chan, and G. Ma, Exceptional nexus with a hybrid topological invariant, *Science* **370**, 1077 (2020).
- [13] R. Su, E. Estrecho, D. Biegaska, Y. Huang, M. Wurdack, M. Pieczarka, A. G. Truscott, T. C. H. Liew, E. A. Ostrovskaya, and Q. Xiong, Direct measurement of a non-Hermitian topological invariant in a hybrid light-matter system, *Sci. Adv.* **7**, eabj8905 (2021).
- [14] W. Zhang, X. Ouyang, X. Huang, X. Wang, H. Zhang, Y. Yu, X. Chang, Y. Liu, D.-L. Deng, and L.-M. Duan, Observation of non-Hermitian topology with nonunitary dynamics of solid-state spins, *Phys. Rev. Lett.* **127**, 090501 (2021).
- [15] K. Wang, A. Dutt, K. Y. Yang, C. C. Wojcik, J. Vukovi, and S. Fan, Generating arbitrary topological windings of a non-Hermitian band, *Science* **371**, 1240 (2021).
- [16] W. Tang, K. Ding, and G. Ma, Direct measurement of topological properties of an exceptional parabola, *Phys. Rev. Lett.* **127**, 034301 (2021).
- [17] K. Wang, A. Dutt, C. C. Wojcik, and S. Fan, Topological complex-energy braiding of non-Hermitian bands, *Nature* **598**, 59 (2021).
- [18] M.-M. Cao, K. Li, W.-D. Zhao, W.-X. Guo, B.-X. Qi, X.-Y. Chang, Z.-C. Zhou, Y. Xu, and L.-M. Duan, Probing complex-energy topology via non-Hermitian absorption spectroscopy in a trapped ion simulator, *Phys. Rev. Lett.* **130**, 163001 (2023).
- [19] Q. Zhang, Y. Li, H. Sun, X. Liu, L. Zhao, X. Feng, X. Fan, and C. Qiu, Observation of acoustic non-Hermitian bloch braids and associated topological phase transitions, *Phys. Rev. Lett.* **130**, 017201 (2023).
- [20] P. Delplace, T. Yoshida, and Y. Hatsugai, Symmetry-protected multifold exceptional points and their topological characterization, *Phys. Rev. Lett.* **127**, 186602 (2021).
- [21] P.-R. Han, W. Ning, X.-J. Huang, R.-H. Zheng, S.-B. Yang, F. Wu, Z.-B. Yang, Q.-P. Su, C.-P. Yang, and S.-B. Zheng, Measuring topological invariants for higher-order exceptional points in quantum three-mode systems, *Nat. Commun.* **15**, 10293 (2024).

* These authors contribute equally to this work.

† E-mail: han_peirong@qq.com

‡ E-mail: zbyang@fzu.edu.cn

§ E-mail: t96034@fzu.edu.cn

[1] M. O. Scully and M. S. Zubairy, *Quantum Optics* (Cambridge, 2000).

[2] C. E. López, G. Romero, F. Lastra, E. Solano, and J. C. Retamal, Sudden birth versus sudden death of entanglement in multipartite systems, *Phys. Rev. Lett.* **101**, 080503 (2008).

[3] S. K. Özdemir, S. Rotter, F. Nori, and L. Yang, Parity-time symmetry and exceptional points in photonics, *Nat.*

[22] H.-L. Zhang, P.-R. Han, X.-J. Yu, S.-B. Yang, J.-H. L, W. Ning, F. Wu, Q.-P. Su, C.-P. Yang, Z.-B. Yang, and S.-B. Zheng, Implementation and topological characterization of weyl exceptional rings in quantum-mechanical systems, *Sci. Bull.* **70**, 2446 (2025).

[23] Y. S. Patil, J. Höller, P. A. Henry, C. Guria, Y. Zhang, L. Jiang, N. Kralj, N. Read, and J. G. Harris, Measuring the knot of non-Hermitian degeneracies and non-commuting braids, *Nature* **607**, 271 (2022).

[24] H. Xu, D. Mason, L. Jiang, and J. G. E. Harris, Topological energy transfer in an optomechanical system with exceptional points, *Nature* **537**, 80 (2016).

[25] J. Doppler, A. A. Mailybaev, J. Böhm, U. Kuhl, A. Girschik, F. Libisch, T. J. Milburn, P. Rabl, N. Moiseyev, and S. Rotter, Dynamically encircling an exceptional point for asymmetric mode switching, *Nature* **537**, 76 (2016).

[26] X.-L. Zhang, S. Wang, B. Hou, and C. T. Chan, Dynamically encircling exceptional points: In situ control of encircling loops and the role of the starting point, *Phys. Rev. X* **8**, 021066 (2018).

[27] W. Liu, Y. Wu, C.-K. Duan, X. Rong, and J. Du, Dynamically encircling an exceptional point in a real quantum system, *Phys. Rev. Lett.* **126**, 170506 (2021).

[28] F. Minganti, A. Miranowicz, R. W. Chhajlany, and F. Nori, Quantum exceptional points of non-Hermitian Hamiltonians and Liouvillians: The effects of quantum jumps, *Phys. Rev. A* **100**, 062131 (2019).

[29] I. I. Arkhipov, A. Miranowicz, F. Minganti, and F. Nori, Liouvillian exceptional points of any order in dissipative linear bosonic systems: Coherence functions and switching between \mathcal{PT} and anti- \mathcal{PT} symmetries, *Phys. Rev. A* **102**, 033715 (2020).

[30] S. Khandelwal, N. Brunner, and G. Haack, Signatures of Liouvillian exceptional points in a quantum thermal machine, *PRX Quantum* **2**, 040346 (2021).

[31] K. Sun and W. Yi, Encircling the Liouvillian exceptional points: a brief review, *AAPPs Bull.* **34**, 22 (2024).

[32] W. Chen, M. Abbasi, Y. N. Joglekar, and K. W. Murch, Quantum jumps in the non-Hermitian dynamics of a superconducting qubit, *Phys. Rev. Lett.* **127**, 140504 (2021).

[33] W. Chen, M. Abbasi, B. Ha, S. Erdamar, Y. N. Joglekar, and K. W. Murch, Decoherence-induced exceptional points in a dissipative superconducting qubit, *Phys. Rev. Lett.* **128**, 110402 (2022).

[34] S. Abo, P. Tulewicz, K. Bartkiewicz, K. zdemir, and A. Miranowicz, Experimental Liouvillian exceptional points in a quantum system without Hamiltonian singularities, *New J. Phys.* **26**, 123032 (2024).

[35] Y.-Y. Chen, K. Li, L. Zhang, Y.-K. Wu, J.-Y. Ma, H.-X. Yang, C. Zhang, B.-X. Qi, Z.-C. Zhou, P.-Y. Hou, *et al.*, Quantum tomography of a third-order exceptional point in a dissipative trapped ion, *Nat. Commun.* **16**, 7478 (2025).

[36] H. Gao, K. Sun, D. Qu, K. Wang, L. Xiao, W. Yi, and P. Xue, Photonic chiral state transfer near the Liouvillian exceptional point, *Phys. Rev. Lett.* **134**, 146602 (2025).

[37] J.-W. Zhang, J.-Q. Zhang, G.-Y. Ding, J.-C. Li, J.-T. Bu, B. Wang, L.-L. Yan, S.-L. Su, L. Chen, F. Nori, *et al.*, Dynamical control of quantum heat engines using exceptional points, *Nat. Commun.* **13**, 6225 (2022).

[38] J.-T. Bu, J.-Q. Zhang, G.-Y. Ding, J.-C. Li, J.-W. Zhang, B. Wang, W.-Q. Ding, W.-F. Yuan, L. Chen, i. m. c. K. Özdemir, F. Zhou, H. Jing, and M. Feng, Enhancement of quantum heat engine by encircling a Liouvillian exceptional point, *Phys. Rev. Lett.* **130**, 110402 (2023).

[39] H.-P. Breuer, E.-M. Laine, J. Piilo, and B. Vacchini, Colloquium: Non-Markovian dynamics in open quantum systems, *Rev. Mod. Phys.* **88**, 021002 (2016).

[40] P.-R. Han, F. Wu, X.-J. Huang, H.-Z. Wu, W. Yi, J. Wen, Z.-B. Yang, and S.-B. Zheng, Characterization of non-Markovianity with maximal extractable qubit-reservoir entanglement, *Appl. Phys. Lett.* **125**, 124003 (2024).

[41] J.-D. Lin, P.-C. Kuo, N. Lambert, A. Miranowicz, F. Nori, and Y.-N. Chen, Non-Markovian quantum exceptional points, *Nat. Commun.* **16**, 1289 (2025).

[42] H.-L. Zhang, P.-R. Han, F. Wu, W. Ning, Z.-B. Yang, and S.-B. Zheng, Experimental observation of non-Markovian quantum exceptional points, *Phys. Rev. Lett.* **135**, 230203 (2025).

[43] Y. Zhou, Z. Zhang, Z. Yin, S. Huai, X. Gu, X. Xu, J. Allcock, F. Liu, G. Xi, Q. Yu, *et al.*, Rapid and unconditional parametric reset protocol for tunable superconducting qubits, *Nat. Commun.* **12**, 5924 (2021).

[44] P.-R. Han, F. Wu, X.-J. Huang, H.-Z. Wu, C.-L. Zou, W. Yi, M. Zhang, H. Li, K. Xu, D. Zheng, H. Fan, J. Wen, Z.-B. Yang, and S.-B. Zheng, Exceptional entanglement phenomena: Non-Hermiticity meeting non-classicality, *Phys. Rev. Lett.* **131**, 260201 (2023).

Supplementary Materials for “Exploring the topology induced by non-Markovian Liouvillian exceptional points”

Hao-Long Zhang^{1,*}, Yan Wang^{1,*}, Wen Ning^{1,*}, Shou-Bang Yang¹, Jia-Hao Lü¹, Fan Wu¹, Pei-Rong Han^{2,†}, Li-Hua Lin^{1,3}, Zhen-Biao Yang^{1,3,‡} and Shi-Biao Zheng^{1,3,§}

¹*Fujian Key Laboratory of Quantum Information and Quantum Optics, College of Physics and Information Engineering, Fuzhou University, Fuzhou 350108, China*

²*School of Physics and Mechanical and Electrical Engineering, Longyan University, Longyan 364012, China*

³*Hefei National Laboratory, Hefei 230088, China*

Contents

Extended Liouvillian matrix and solution of the secular equation	1
Eigenvalues extraction	4
Trajectories of the measured Liouvillian eigenvalues associated with the LEP3	5
References	6

EXTENDED LIOUVILLIAN MATRIX AND SOLUTION OF THE SECULAR EQUATION

The dynamics of the entire Q-PM system can be described by the Lindblad master equation

$$\frac{\partial \rho}{\partial t} = -i[H, \rho] + \kappa b \rho b^\dagger - \frac{\kappa}{2} \{b^\dagger b, \rho\} \equiv \mathcal{L} \rho, \quad (\text{S1})$$

where the system Hamiltonian is given by $H = g(b^\dagger|g\rangle\langle e| + b|e\rangle\langle g|) + \Delta|e\rangle\langle e|$, the system state ρ is a 3×3 density matrix in the subspace $\{|g, 0\rangle, |e, 0\rangle, |g, 1\rangle\}$, and the extended Liouvillian superoperator \mathcal{L}_{matrix} in the defined matrix representation can be written as

$$\begin{aligned} \mathcal{L}_{matrix} &= -i(H \otimes I - I \otimes H^\top) + \frac{\kappa}{2} (2b \otimes b^* - b^\dagger b \otimes I - I \otimes b^\top b^*) \\ &= -i(H \otimes I - I \otimes H^\top) + \frac{\kappa}{2} (2b \otimes b - b^\dagger b \otimes I - I \otimes b^\dagger b). \end{aligned} \quad (\text{S2})$$

Here \otimes is the Kronecker product operation, \top and $*$ represent the transpose and complex conjugate operations, respectively. Therefore, in the subspace spanned by $\{|g, 0\rangle, |e, 0\rangle, |g, 1\rangle\}$, the matrix form of the extended Liouvillian superoperator is a 9×9 matrix:

$$\mathcal{L}_{matrix} = \begin{pmatrix} 0 & 0 & 0 & 0 & 0 & 0 & 0 & 0 & \kappa \\ 0 & i\Delta & ig & 0 & 0 & 0 & 0 & 0 & 0 \\ 0 & ig & -\frac{\kappa}{2} & 0 & 0 & 0 & 0 & 0 & 0 \\ 0 & 0 & 0 & -i\Delta & 0 & 0 & ig & 0 & 0 \\ 0 & 0 & 0 & 0 & ig & 0 & -ig & 0 & 0 \\ 0 & 0 & 0 & ig & -\frac{\kappa}{2} - i\Delta & 0 & 0 & -ig & 0 \\ 0 & 0 & 0 & -ig & 0 & 0 & -\frac{\kappa}{2} & 0 & 0 \\ 0 & 0 & 0 & 0 & -ig & 0 & 0 & -\frac{\kappa}{2} + i\Delta & ig \\ 0 & 0 & 0 & 0 & -ig & 0 & ig & 0 & -\kappa \end{pmatrix}. \quad (\text{S3})$$

By solving the secular equation

$$\mathcal{L}_{matrix} \mathbf{V}_j = \lambda_j \mathbf{V}_j, \quad (\text{S4})$$

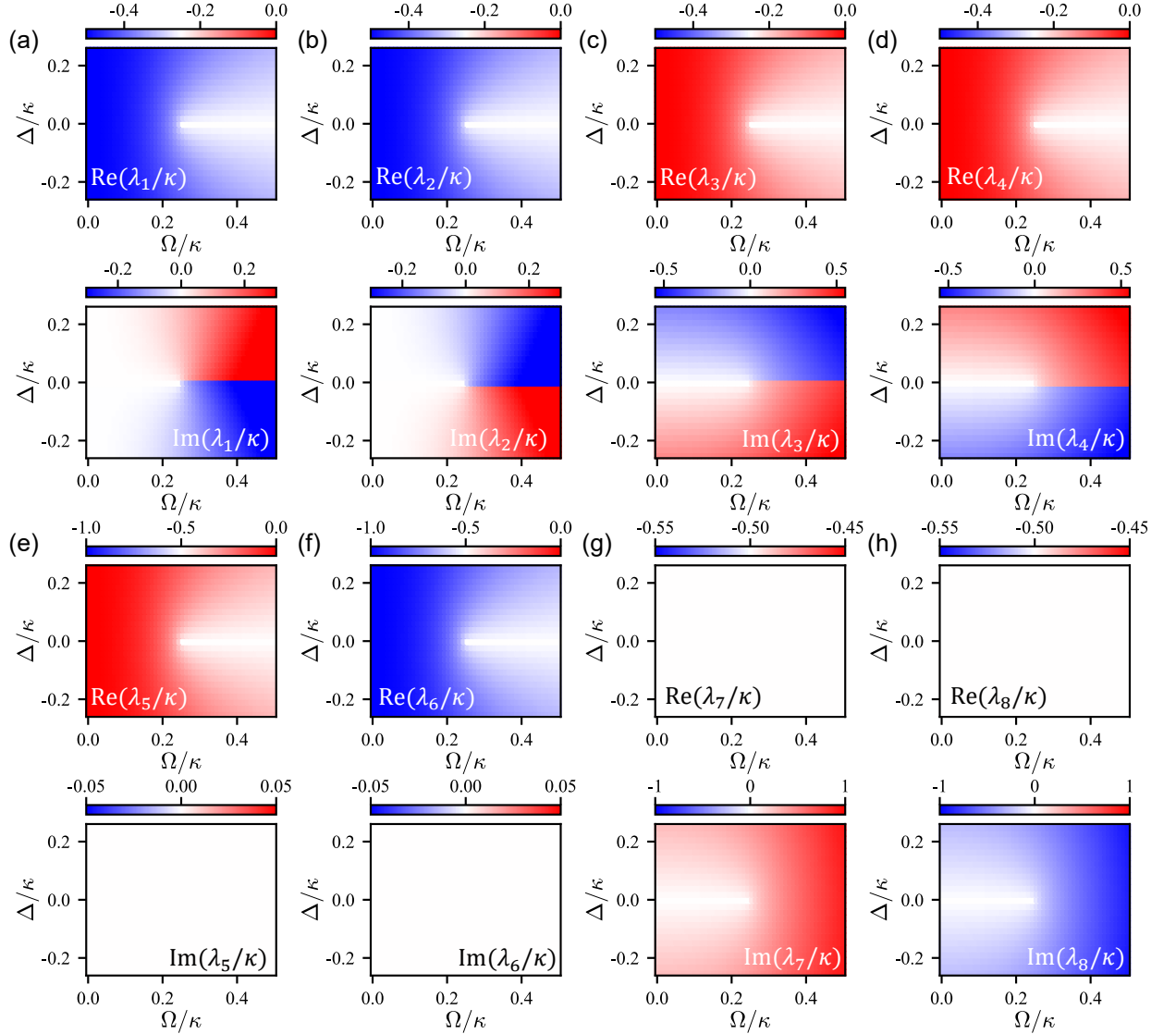


FIG. S1: (color online). Liouvillian spectrum for the theoretical model. (a)-(h) The last eight eigenvalues of the extended Liouvillian superoperator, λ_1 to λ_8 , versus the control parameters Ω and Δ . The first eigenvalue λ_0 remains to be 0, irrespective of Ω and Δ (in unit of κ).

the eigenvalues λ_j and the eigenvectors \mathbf{V}_j (represented by the density matrix form ρ_j) of the extended Liouvillian superoperator can be obtained, written as follows:

$$\lambda_0 = 0, \quad \mathbf{V}_0 = (1 \ 0 \ 0 \ 0 \ 0 \ 0 \ 0 \ 0 \ 0 \ 0)^T; \quad (S5)$$

$$\lambda_1 = \eta_- - \sqrt{\eta_+^2 - \Omega^2}, \quad \mathbf{V}_1 = \frac{1}{N_1} \left[0 \ 0 \ 0 \ -i(\eta_+ + \sqrt{\eta_+^2 - \Omega^2}) \ 0 \ 0 \ \Omega \ 0 \ 0 \right]^T; \quad (S6)$$

$$\lambda_2 = \eta_+ - \sqrt{\eta_-^2 - \Omega^2}, \quad \mathbf{V}_2 = \frac{1}{N_2} \left[0 \ i(\eta_- + \sqrt{\eta_-^2 - \Omega^2}) \ \Omega \ 0 \ 0 \ 0 \ 0 \ 0 \ 0 \ 0 \right]^T; \quad (S7)$$

$$\lambda_3 = \eta_- + \sqrt{\eta_+^2 - \Omega^2}, \quad \mathbf{V}_3 = \frac{1}{N_3} \begin{bmatrix} 0 & 0 & 0 & -i(\eta_+ - \sqrt{\eta_+^2 - \Omega^2}) & 0 & 0 & \Omega & 0 & 0 \end{bmatrix}^T; \quad (S8)$$

$$\lambda_4 = \eta_+ + \sqrt{\eta_-^2 - \Omega^2}, \quad \mathbf{V}_4 = \frac{1}{N_4} \begin{bmatrix} 0 & i(\eta_- - \sqrt{\eta_-^2 - \Omega^2}) & \Omega & 0 & 0 & 0 & 0 & 0 & 0 \end{bmatrix}^T; \quad (S9)$$

$$\lambda_5 = -\frac{\kappa}{2} + \sqrt{\alpha + \beta}, \quad \mathbf{V}_5 = \frac{1}{N_5} \begin{bmatrix} \frac{\kappa}{\lambda_5} \\ 0 \\ 0 \\ 0 \\ \frac{1}{16\Omega^2} \left(\kappa^2 + 8\beta + 4\kappa\sqrt{\alpha + \beta} + \Delta^2 \left(\frac{4\sqrt{\alpha + \beta} + 4\kappa}{\sqrt{\alpha + \beta}} \right) \right) \\ \frac{i\sqrt{2}(-16\Omega^2 + 8\beta) + (2\Delta + i\kappa)(-2i\sqrt{2}\Delta + \sqrt{2}\kappa + 4\sqrt{2}\sqrt{\alpha + \beta})}{16\sqrt{2}\Omega\sqrt{\alpha + \beta}} \\ 0 \\ \frac{1}{8\Omega} \left(\Delta \left(\frac{4\sqrt{\alpha + \beta} + 2\kappa}{\sqrt{\alpha + \beta}} \right) - i(2\kappa + 4\sqrt{\alpha + \beta}) \right) \\ 1 \end{bmatrix}; \quad (S10)$$

$$\lambda_6 = -\frac{\kappa}{2} - \sqrt{\alpha + \beta}, \quad \mathbf{V}_6 = \frac{1}{N_6} \begin{bmatrix} \frac{\kappa}{\lambda_6} \\ 0 \\ 0 \\ 0 \\ \frac{1}{16\Omega^2} \left(\kappa^2 + 8\beta - 4\kappa\sqrt{\alpha + \beta} + \Delta^2 \left(\frac{4\sqrt{\alpha + \beta} - 4\kappa}{\sqrt{\alpha + \beta}} \right) \right) \\ \frac{1}{8\Omega} \left(4\Delta + 2i\kappa - \frac{2\Delta\kappa}{\sqrt{\alpha + \beta}} - 4i\sqrt{\alpha + \beta} \right) \\ 0 \\ \frac{1}{8\Omega} \left(\Delta \left(\frac{4\sqrt{\alpha + \beta} - 2\kappa}{\sqrt{\alpha + \beta}} \right) - i(-2\kappa + 4\sqrt{\alpha + \beta}) \right) \\ 1 \end{bmatrix}; \quad (S11)$$

$$\lambda_7 = -\frac{\kappa}{2} + \sqrt{\alpha - \beta}, \quad \mathbf{V}_7 = \frac{1}{N_7} \begin{bmatrix} \frac{\kappa}{\lambda_7} \\ 0 \\ 0 \\ 0 \\ \frac{1}{16\Omega^2} \left(\kappa^2 - 8\beta - 4\kappa\sqrt{\alpha - \beta} + \Delta^2 \left(\frac{4i\sqrt{\alpha - \beta} + 4\kappa}{\sqrt{\alpha - \beta}} \right) \right) \\ \frac{i\sqrt{2}(16\Omega^2 + 8\beta) + (2\Delta + i\kappa)(-2i\sqrt{2}\Delta + \sqrt{2}\kappa + 4\sqrt{2}\sqrt{\alpha - \beta})}{16\sqrt{2}\Omega\sqrt{\alpha - \beta}} \\ 0 \\ \frac{1}{8\Omega} \left(\Delta \left(\frac{4\sqrt{\alpha - \beta} - 2\kappa}{\sqrt{\alpha - \beta}} \right) + i(-2\kappa + 4\sqrt{\alpha - \beta}) \right) \\ 1 \end{bmatrix}; \quad (S12)$$

$$\lambda_8 = -\frac{\kappa}{2} - \sqrt{\alpha - \beta}, \quad \mathbf{V}_8 = \frac{1}{N_8} \begin{bmatrix} \frac{\kappa}{\lambda_8} \\ 0 \\ 0 \\ 0 \\ \frac{1}{16\Omega^2} \left(\kappa^2 - 8\beta + 4\kappa\sqrt{\alpha - \beta} + \Delta^2 \left(\frac{4\sqrt{\alpha - \beta} + 4\kappa}{\sqrt{\alpha - \beta}} \right) \right) \\ \frac{1}{8\Omega} \left(4\Delta + 2i\kappa - \frac{2\Delta\kappa}{\sqrt{\alpha - \beta}} - 4i\sqrt{\alpha + \beta} \right) \\ 0 \\ \frac{1}{8\Omega} \left(\Delta \left(\frac{4\sqrt{\alpha - \beta} + 2\kappa}{\sqrt{\alpha - \beta}} \right) - i(2\kappa + 4\sqrt{\alpha - \beta}) \right) \\ 1 \end{bmatrix}. \quad (S13)$$

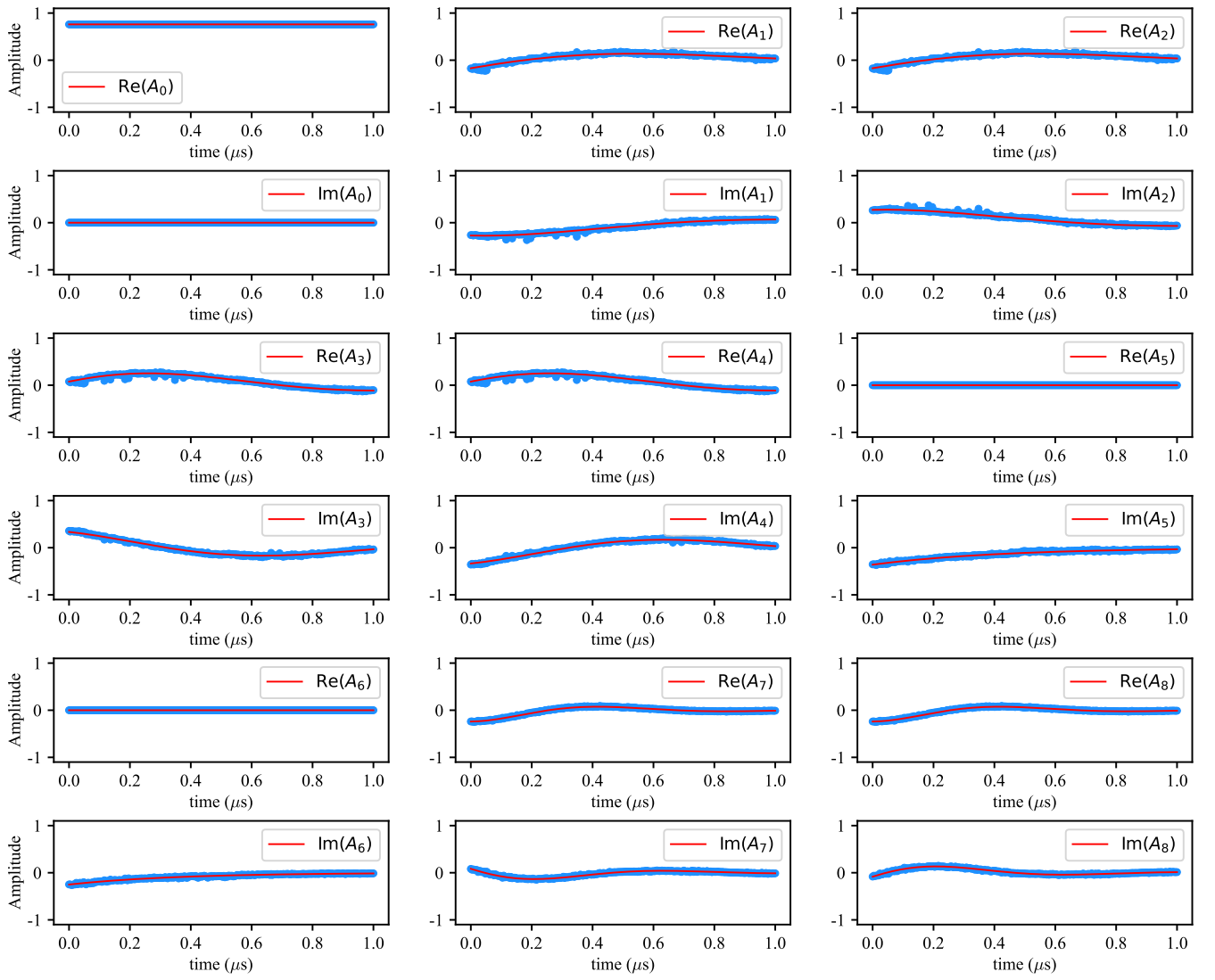


FIG. S2: The real and imaginary parts of the amplitudes associated with the eigenmatrices $A_j(t)$ versus the evolution time t , for $g/2\pi \approx 0.620$ MHz and $\Delta/2\pi \approx 0.150$ MHz. Dots and lines denote the experimentally measured and fitting results, respectively.

Here $\eta_{\pm} = \frac{1}{4}(-\kappa \pm 2i\Delta)$, $\alpha = \kappa^2/8 - \Delta^2/3 - 2\Omega^2$, $\beta = \sqrt{\alpha^2 + \Delta^2\kappa^2/4}$ and N_j ($j = 1, 2, \dots, 8$) are the normalization constants.

The last eight eigenvalues versus the coupling strength Ω and detuning Δ are displayed in Fig. S1(a)-(h), where the upper and lower panels in each subfigure respectively denote the real and imaginary parts of the corresponding eigenvalue.

EIGENVALUES EXTRACTION

The eigenvalues of the Liouvillian superoperator can be extracted by fitting the time evolution of the amplitude $A_j(t)$, as shown in Eq. (8) in the main text. In our experiment, the system state $\rho(t)$ at each moment can be reconstructed via quantum state tomography and expressed in terms of the superoperator $\mathbf{V}(t)$. To obtain the amplitude $A_j(t)$, we numerically compute the left eigenmatrices (\mathbf{T}_j) of the Liouvillian superoperator (\mathcal{L}_{matrix}) by solving

$$\mathcal{L}_{matrix}^{\dagger} \mathbf{T}_j = \lambda_j^* \mathbf{T}_j. \quad (\text{S14})$$

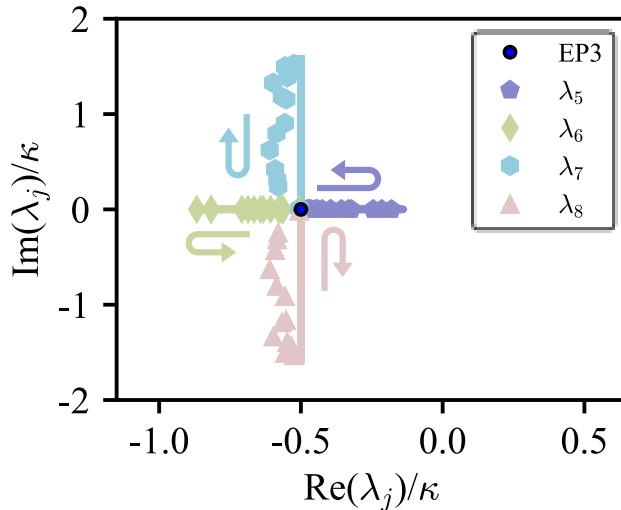


FIG. S3: (color online). Trajectories of the measured Liouvillian eigenvalues: λ_5 , λ_6 , λ_7 , and λ_8 are plotted on the complex $\text{Re}(\lambda)$ - $\text{Im}(\lambda)$ plane (in unit of κ). The control parameters are varied along the circle shown in the main text. The solid lines denote the trajectories of the calculated eigenvalues.

The amplitude $A_j(t)$ is then extracted by left-multiplying $\mathbf{V}(t)$ with \mathbf{T}_j^\dagger , according to the biorthogonal condition $\mathbf{T}_i^\dagger \mathbf{V}_j = \delta_{ij}$. Through identifying the information of all the components of the density matrix $\rho(t)$ at different times, and then with resorting to the least-square method for using the obtained $A_j(t)$ to fit the exponential function $C_j e^{Bt}$, we can get the best-fit eigenvalues, i.e., $B = \lambda_j$.

Under the circumstances, the error function is defined as [1, 2]

$$\text{Erf} = |A_j(t) - C e^{Bt}|^2. \quad (\text{S15})$$

The best-fit eigenvalues λ_j are then the values minimizing the error function of (S15). The experimentally measured $A_j(t)$ (dots) and their fitting results (lines) are given in Fig. S2.

TRAJECTORIES OF THE MEASURED LIOUVILLIAN EIGENVALUES ASSOCIATED WITH THE LEP3

The problem remains of whether or not the other eigenvalues can also display topological features. Neither \mathbf{V}_0 nor \mathbf{V}_8 coalesces with any other eigenvector, and thus they have nothing to do with the EPs. Consequently, the corresponding eigenvalues λ_0 and λ_8 do not exhibit any topological effect. On the other hand, \mathbf{V}_5 , \mathbf{V}_6 , and \mathbf{V}_7 coalesce at the parameter-space point $\Omega = \kappa/2$; $\Delta = 0$. For an HEP3, the spectral winding number defined by Eq. (8) in the main text is $\pm 1/3$ [3]. However, this is not the case for the non-Markovian LEP3. To illustrate this point, we present λ_5 , λ_6 , and λ_7 in Fig. S3, which shows that these eigenvalues move back and forth along the real or imaginary axis, without traversing any closed path, when k is varied from 0 to 2π . Consequently, the winding numbers associated with these eigenvalues are also zero. The topology associated with an EP3 can also be quantified by the homotopy invariant, calculated in terms of the resultant vector [1].

The resultant vector $\mathbf{R} = (R_1, R_2)$ is defined by the resultant,

$$R_{P_1, P_2} = \det S_{P_1, P_2}, \quad (\text{S16})$$

where S_{P_1, P_2} is the Sylvester matrix, and P_i can be obtained by the characteristic polynomial P ,

$$P_i = \frac{\partial}{\partial \lambda} P, \quad (\text{S17})$$

where $P = -\prod_{i=1}^9 (\lambda - \lambda_i)$. The components of the resultant vector are defined as

$$\begin{aligned} R_1 &= R_{P_0, P_1}, \\ R_2 &= R_{P_0, P_2}. \end{aligned} \quad (\text{S18})$$

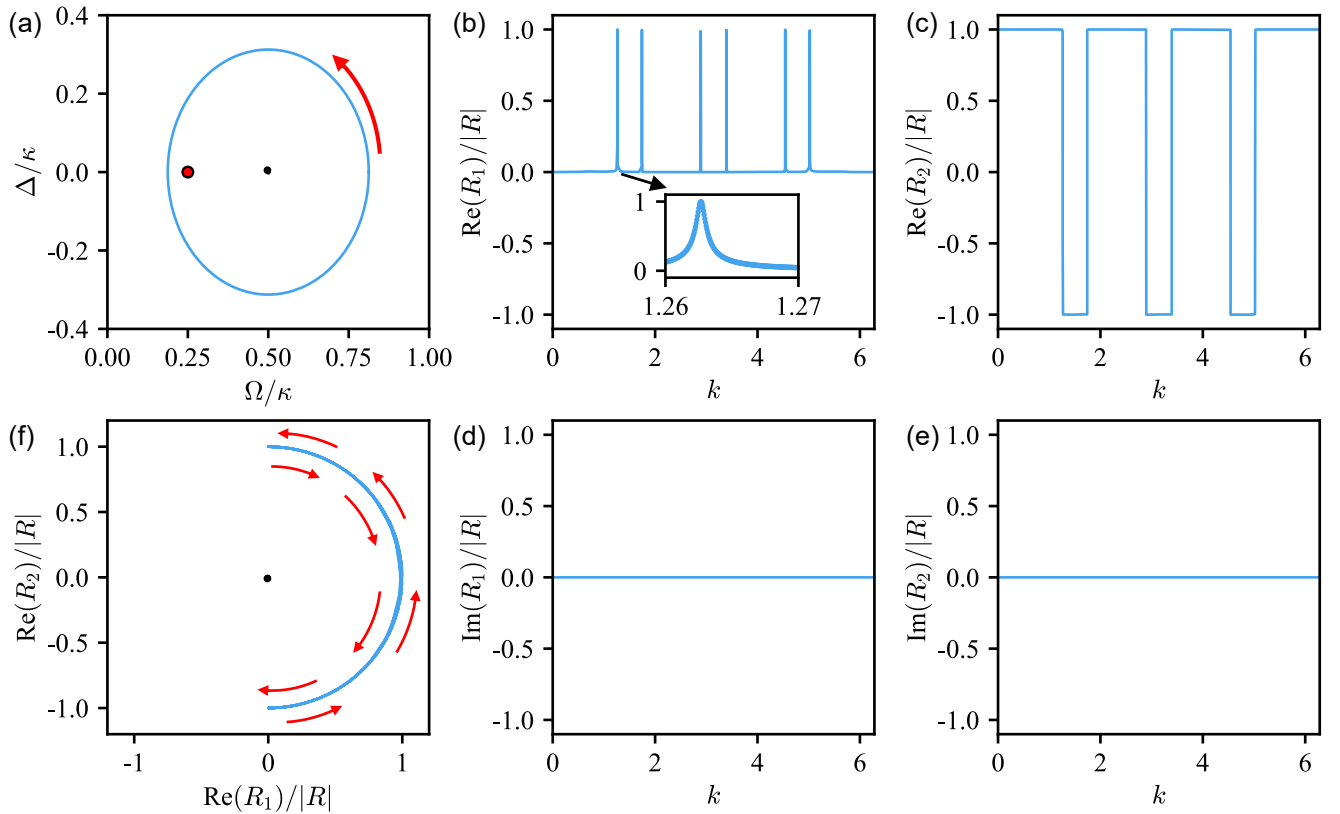


FIG. S4: (a) Parameter-space loop. We here set $\Omega = \kappa/2 + r \cos k$ and $\Delta = r \sin k$, so that the LEPs (dot), located at $\{r = \kappa/4, k = \pi\}$, are enclosed in the loop when $r > \kappa/4$. (b)-(e) The components of the resultant vectors with respect to k . (f) Trajectory of the rescaled resultant vector on the plane of $[\text{Re}(R_1)/|R|, \text{Re}(R_2)/|R|]$.

For an HEP3, such an invariant has a value of ± 1 , as has been theoretically predicted [4] and experimentally demonstrated [1]. To obtain the homotopy invariant of LEP3s, we numerically calculate the resultant vector along a closed path in the parameter space, as shown in Fig. S4(a). The components of the resultant vector as a function of k are displayed in Fig. S4(b)-(e). It can be seen that the resultant vector just makes a trivial back-and-forth movement even when the control parameter is varied along a closed path, as shown in Fig. S4(f). This means that the homotopy invariant for the non-Markovian LEP3 is zero.

* These authors contribute equally to this work.

† E-mail: han_peirong@qq.com

‡ E-mail: zbyang@fzu.edu.cn

§ E-mail: t96034@fzu.edu.cn

[1] P.-R. Han, W. Ning., X.-J. Huang, et al. Nat. Commun. 15, 10293 (2024).

[2] H.-L. Zhang, P.-R. Han, F. Wu., et al. Phys. Rev. Lett. 135, 230203 (2025).

[3] Y.-Y. Chen, K. Li, L. Zhang, et al. Nat. Commun 16, 7478 (2025).

[4] P. Delplace, T. Yoshida, and Y. Hatsugai. Phys. Rev. Lett. 127, 186602 (2021)